Research Article Vol. 17, No. 7 / 1 Jul 2026 / Biomedical Optics Express 3502
Biomedical Optics EXPRESS

Quantification and mitigation of system background fluorescence in fiber-optic-based imaging systems

ERIC BRACE,[1,2,*] JEANIE MALONE,[1] ADRIAN TANSKANEN,[1] LAURA PAULUS,[1,3] KEVIN BENNEWITH,[1,3,4] CALUM MACAULAY,[1,4] AND PIERRE LANE[1,2,5]

[1]Basic & Translational Research, British Columbia Cancer Research Institute, Vancouver, BC, Canada
[2]School of Engineering Science, Simon Fraser University, Burnaby, BC, Canada
[3]Interdisciplinary Oncology Program, University of British Columbia, Vancouver, BC, Canada
[4]Department of Pathology and Laboratory Medicine, University of British Columbia, Vancouver, BC, Canada
[5]School of Biomedical Engineering, University of British Columbia, Vancouver, BC, Canada
[*]ebrace@bccrc.ca

Abstract: Autofluorescence imaging provides a snapshot of tissue biochemistry that can be used to identify dysplastic tissue. However, deployment in multimodal single-fiber imaging systems is limited by system background fluorescence. We propose to improve the signal-to-background ratio (SBR) through the removal of background emission in fiber-optic catheters for autofluorescence and optical coherence tomography. We collected power and spectral measurements of optical components to characterize their emissions using 450 nm excitation. We measured the per-meter fluorescence contribution of single-mode, double-clad, and multimode optical fibers. By tailoring the detection filter to the emission spectra of the target tissue and system background, we have demonstrated an average of 7.9x improvement in SBR.

1. Introduction

Biological fluorescence is achieved through absorption of light by fluorophores within tissue which is then re-emitted at lower energy (longer wavelength) [1]. These fluorophores are classified as endogenous (originating in the biological tissue) or exogenous (originating outside the tissue, such as contrast agents or dyes). Autofluorescence Imaging (AFI) refers to excitation and collection of fluorescent emission from endogenous fluorophores and can provide insight into the tissue biochemical state [2]. Although this method generally results in weaker fluorescence intensity, it avoids potential allergic or toxic adverse events arising from exogenous dyes [3–6] and does not require regulatory approval. Further, use of exogenous fluorophores generally results in selectively targeting a limited number of compounds, restricting the ability to collect information about other potential responses occurring in the tissue.

When excited with blue light (~450 nm), human tissue has been shown to emit green fluorescence (~550 nm) that reduces in intensity during neoplastic progression compared to surrounding tissue [7–12]. Tissue around dysplastic epithelium also emits more red than green fluorescence [9,13]. Autofluorescence intensity of cancerous oral tissue has approximately one third that of healthy tissue under 375–440 nm excitation light [14]. This loss of autofluorescence has been shown to be a high sensitivity detection method that correlates to neoplastic growth in various organ sites, including oral, lung, cervix, colon, and esophagus [15–25].

Biopsy guidance for the diagnostic confirmation of cancer is an important application of AFI. Throughout dysplastic progression, tissue can undergo a number of changes such as collagen remodeling, inflammation, vascular growth, and deregulated metabolism [26–28]. Dysplastic

#597273 https://doi.org/10.1364/BOE.597273
Journal © 2026 Received 16 Mar 2026; revised 23 May 2026; accepted 26 May 2026; published 9 Jun 2026

Biomedical Optics EXPRESS

progression can be subtle and challenging to visually identify during clinical screening and diagnosis. Clinically occult lesions can be visualized with AFI, compared to white light inspection alone, which may result in collection of biopsies from malignancies that may otherwise have appeared benign [13, 23, 29–34]. Handheld imaging tools benefit from simple deployment and have seen clinical success, particularly in oral applications. Dysplastic progression in internal organs present similar challenges, requiring catheters for endoscopic applications of AFI to assess small diameter sites. Fiber optics enable fabrication of thin and flexible tools to guide light to and from internal organs, expanding the clinical applications of AFI to sites such as the lung, cervix, and colon.

Although autofluorescence is a high sensitivity tool for biochemical abnormalities, it is subject to low specificity, where inflammation may present with reduced fluorescence response similarly to dysplasia [35]. When used in conjunction with AFI, Optical coherence tomography (OCT) may assist in identifying AFI false positives through simultaneous assessment of tissue structure and stratification [36,37]. OCT is an imaging method that measures pathlength differences between the target and a reference to generate high resolution structural imaging. With this information, one can assess tissue structure to identify abnormalities associated with dysplasia such as epithelial thickening and changes in attenuation. Small-diameter (~1 mm) OCT catheters using rotary pullback circumferential-scanning devices or piezoelectric forward-scanning implementations have been shown to have clinical applications, such as biopsy guidance, screening, and disease monitoring [38]. Multimodal approaches further expand the capabilities of these devices, leveraging additional optical technologies such as polarization sensitivity, angiography, spectroscopy, elastography, and fluorescence imaging [39,40].

We previously developed a multimodal optical imaging system which merged blue-light (450 nm excitation) AFI with OCT in a single-fiber catheter using double-clad fiber (DCF) catheters [41,42]. Imaging catheters are limited to a single fiber when accessing small diameter organs, such as the lungs or fallopian tubes, preventing separation of excitation and collection pathways. The DCF used in these catheters combine a narrow and low numerical aperture (NA) core to transmit both the excitation signal and the infrared OCT signal, with a wide diameter and high NA inner-cladding to collect the low intensity AF emissions from tissue. A double-clad fiber coupler (DCFC) directs excitation light to the sample along the core of a DCF fiber and returns emissions to a single photodetector by separating light traveling in the inner-cladding.

This system was demonstrated to be capable of *in vivo* clinical lung imaging, successfully distinguishing pathological grades of lesions and visualizing blood vessels [41]. However, low SBR caused inconsistent imaging quality that varied widely based on catheter fabrication tolerance and acquisition environment. The contribution of tissue fluorescence to the measured intensity was often small relative to that of system background fluorescence, resulting in high signals with small differences that are susceptible to instability due to Poisson statistics. This makes comparison between disease states and performing longitudinal studies challenging.

Endogenous fluorescence is not unique to biological samples; fluorescence can also arise from the internal optics used in these imaging tools. Photonic emissions inherent to the device appear as background which can be on the same order of magnitude as the low intensity tissue autofluorescence signal. This results in measurements with a low signal-to-background ratio (SBR). SBR provides a quantitative metric to assess image contrast, defined by,

$$\mathrm{SBR} = \frac{P_{\mathrm{signal}}}{P_{\mathrm{background}}} = \frac{P_{\mathrm{total}} - P_{\mathrm{background}}}{P_{\mathrm{background}}}, \tag{1}$$

where P_{total} is the total measured fluorescence power at the detector and $P_{\mathrm{background}}$ is the measured background fluorescence power without a target present.

Autofluorescence signals are also subject to degradation through detector dark current and noise. Dark current can be accounted for by measuring and subtracting the detector level without

Biomedical Optics EXPRESS

activation of the source [43]. Shot noise can be mitigated by collecting a high number of photons, which minimizes impact of the random arrival [43]. Post-processing (contrast stretching) can be applied to improve image contrast by adjusting the black level but there is a risk that weak tissue fluorescence is obfuscated by the system background emission. Poor SBR and high noise results in low contrast and inability to resolve image features.

Germanium (Ge^+) and fluorine (F^-) are commonly used dopants within optical fibers. Germanium is well understood to be a source of system fluorescence [44–47]. As excitation light passes through the optical fiber, it excites these alterations used to modify the fiber refractive index profile [48–52]. Pure silica, conversely, exhibits little to no fluorescence making it an ideal material for reduction of system background.

In single-fiber DCF catheters, excitation light travels along the core (Ge^+ doped) toward the target tissue; tissue fluorescence is collected and travels in the opposite direction in the core and inner-cladding (pure silica), the latter of which is separated by the DCFC leading to the detector (Fig. 1 a). The intensity of fiber-generated fluorescence produced in the core of a DCF and subsequently coupled into its inner-cladding is proportional to: (1) the dopant concentration in the core; (2) the length of the fiber; and (3) the recapture factor of the inner-cladding [45,53].

The maximum possible background incident upon the detector is defined by the emissions captured by the inner-cladding of the DCF along the return path. We assume the spontaneous emission of the dopants act as a point source, isotopically radiating light. Thus, the fraction of collected background is related to the solid angle of a cone subtended by the internal transmission angle of the fiber (Fig. 1 b, c),

$$\Omega = 4\pi \left(\sin^2 \left(\frac{\theta_t}{2} \right) \right) = 2\pi(1 - \cos\theta_t), \tag{2}$$

where $\theta_t = \cos^{-1}\left(\frac{n_{clad}}{n_{core}}\right)$ defines the transmission angle, and n_{core}, n_{clad} are the refractive indices of the optical fiber core and cladding, respectively (Fig. 1 b, c). The autofluorescence recapture factor in the core of a step index optical fiber can then be approximated as,

$$S_{\text{core}} = \frac{\Omega}{4\pi} \cong \frac{1}{4}\left(\frac{NA_{\text{core}}}{n_{\text{core}}}\right)^2. \tag{3}$$

The remaining fluorescence is either coupled by the core in the forward direction or emitted out the side of the fiber. The portion of emission collected by the (inner) cladding in the backward direction is,

$$S_{\text{clad}} \cong \frac{1}{4}\left(\left(\frac{NA_{\text{clad}}}{n_{\text{clad}}}\right)^2 - \left(\frac{NA_{\text{core}}}{n_{\text{core}}}\right)^2\right), \tag{4}$$

where we assume any emission collected by the core does not reach the inner-cladding. Based on published index of refraction data for a commercially available DCF (DCF 13, Thorlabs, New Jersey) [54], we estimate 0.17% of emitted light would be coupled into single mode fiber (SMF) and DCF cores (Eq. (3)), while 0.31% would be coupled into the DCF inner-cladding (Eq. (4)).

Based on the common dopant profiles of SMF, and DCF fibers (Fig. 1 d, f), we expect the germanium doped core in SMF and DCF to emit fluorescence. A portion of this fluorescence is then collected in the core and cladding of the fiber. As MMF cores are generally pure silica (Fig. 1 (e)), little fluorescence intensity is expected. We posit that selection of appropriate fibers (and lengths thereof) is critical for minimizing fluorescence background emission and therefore optimizing device performance.

Efforts have been made to characterize and mitigate fluorescence in fiber optic devices using spectral unmixing techniques [55]. However, this approach requires very fast collection of spectral data and longer acquisition times than single photodetector-based approaches to collect

Biomedical Optics EXPRESS

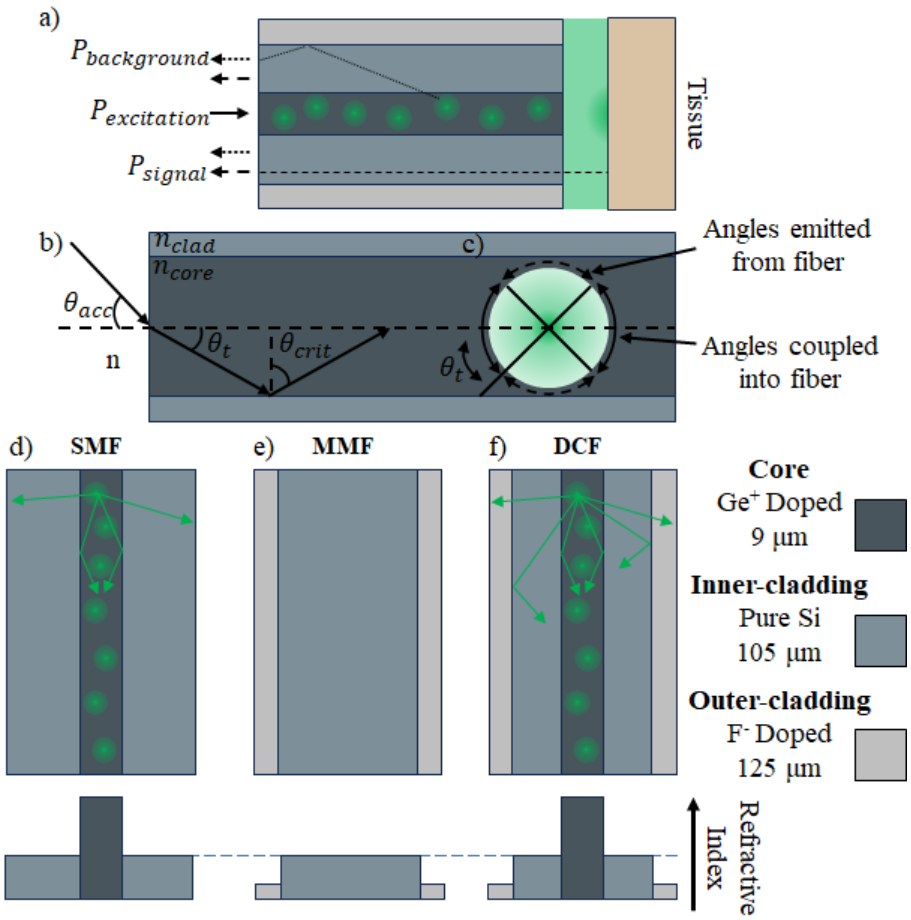

Fig. 1. Fiber dopant emission and collection. a) illustration of power propagation through DCF: showing excitation propagating through the core, tissue signal and system background propagating through the inner-cladding b) fiber optic propagation geometry: showing the relationship between the fiber acceptance angle, the transmission angle, and the critical angle c) dopant emission and collection model: showing the uniform distribution of fluorescence emission and the relationship to the transmission angle d, e, f) visualizations of SMF, MMF, and DCF dopant profiles and dopant emission behavior.

sufficient photons. The same group also presented a low fluorescence optimized imaging system using a 3D printed lens showing detection of carotid plaque autofluorescence under 633 nm excitation [56]. It is understood that optical fibers fluoresce under visible light excitation, which has been quantified for excitation wavelengths ranging from 250 to 650 nm [45]. A recent study explored the spectra of commercial fiber autofluorescence for 520 nm excitation magnetic sensors [57]. To our knowledge, there is currently limited published data quantifying single optical fiber and system component fluorescence behavior under 450 nm excitation, and their impacts on AFI SBR.

Implementation and optimization of tools capable of utilizing autofluorescence detection provides a promising avenue for high sensitivity identification of dysplastic tissue and biopsy guidance. The end-goal of this work is to detect AFI using a single photodetector as the integration time required for a spectroscopic approach is not practical for high rotation speed catheter applications. Additionally, system fluorescence reaching the detector can vary with fiber

Biomedical Optics EXPRESS

optic rotary joint (FORJ) coupling and inclusion of highly reflective objects in the sample path [55]. Intensity normalization is a challenge with AFI, as excitation light is incident on different compositions of endogenous fluorophores throughout the pullback; clinical utility of the device depends on the ability to distinguish dysplasia from normal tissue.

This work aims to characterize spectral contributions of common optical components deployed in fiber optic imaging systems utilizing 450 nm (blue) excitation. Spectral and power contributions are quantified per-meter of optical fiber, as well as for DCFC and FORJ. Based on our results, we demonstrate targeted spectral filtering and component replacements to reduce background fluorescence contributions in an OCT-AFI system.

2. Materials and methods

The approach of this work centers around iterative exploration and implementation of findings to inform later experimental stages. We began by first characterizing and optimizing the measurement system and fiber sample preparation methods. We then measured the fluorescence power and spectra characteristics of a selection of optical fibers. Finally, we applied our observations to a catheter-based OCT-AFI system to quantify improvements. The design of the fluorescence measurement system used the same components as the AFI subsystem of our clinical OCT-AFI system.

A sample in this work refers to a length of fiber used for fluorescence testing; lengths, index profiles, coatings, and jacketing vary depending on the experiment. Unless otherwise stated: all methods were assessed with 1 mW of 450 nm continuous excitation input to Port A of the DCFC, additionally, all fibers were connectorized in SC/APC packaging (F1-3069APC, Fiber Instrument Sales, New York) using blue dye epoxy (FIS T60-065-B2, Fiber Instrument Sales, New York) with ~1 cm of coating stripped from the tip of the fiber. We observed negligible difference in sample fluorescence when comparing various commercially available connector epoxies compared to the background generated by 2 m of DCF under continuous illumination. Variations in intensity were within previously observed connect-reconnect variability.

2.1. Catheter system

The OCT-AFI system consists of a wavelength division multiplexer (WDM) (WD202A2, Thorlabs, New Jersey), a standard (not fluorescence optimized) DCFC (DC1300LEFA, Thorlabs, New Jersey), FORJ (MJXA-SAPB-131-DC-015-FA-8, Princetel, New Jersey), and a custom imaging catheter, along with adjoining optical fibers between each component (Fig. 2).

The FORJ is an interface between the static and rotating fiber optic components, which allows for circumferential scanning with the catheter. The specifications report an insertion loss of <2 dB, with a variability of <±0.25 dB between 650–1650 nm [58]. It contains a proprietary coupling fluid within the optical path, the impact of which cannot be accounted for as the fluorescence properties are unavailable.

The optical path of the custom catheter (described in [41]) consists of 1.65 m of DCF, a 425 μm (nominal length) multimode fiber expansion spacer, a 62 μm length of gradient index fiber focusing lens, and a no core fiber reflector polished to 53° (Fig. 2 inset). The tip of the spliced optical fiber is encased in a 12.7 μm layer of polyester shrink tubing (Nordson Medical, Ohio) that extends past the reflecting surface, the end of which is sealed with UV-cure epoxy (NOA 63, Norland Products Inc. Jamesburg, New Jersey). This forms an air cavity that generates total internal reflection to redirect the beam circumferentially. Polyester shrink tubing with a thickness of 25.4 μm (Nordson Medical, Ohio) is affixed to the end of a torque coil, which the fiber is then inserted into. The reflector tip is then secured within the torque coil and shrink tubing by filling the cavity with UV-cure epoxy (resulting in 191 μm of epoxy within the optical path). During imaging, the optical assembly is inserted into a 100 μm thick polyether block amide (PEBAX) window tube (Rose Medical, Michigan) which is filled with water.

Biomedical Optics EXPRESS

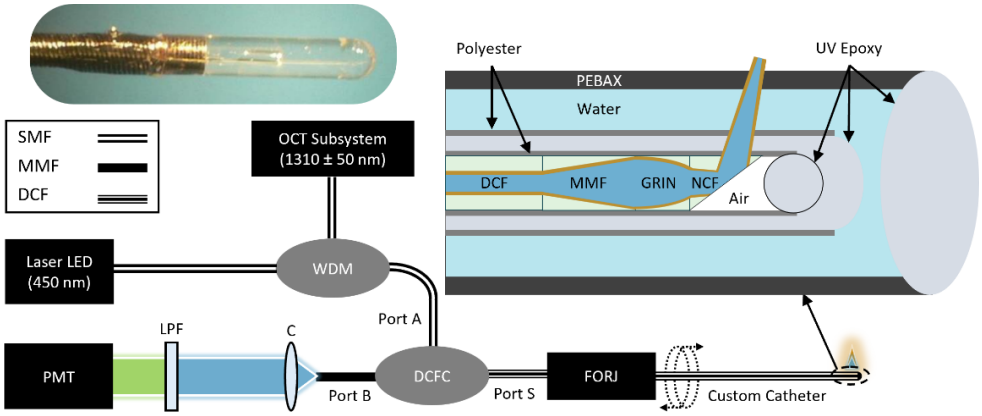

Fig. 2. Optical schematic of OCT-AFI system. WDM, wavelength division multiplexer; DCFC, double-clad fiber coupler; LPF, long pass filter; PMT, photomultiplier tube; FORJ, fiber optic rotary joint; SMF, single mode fiber; MMF, multimode fiber; DCF, double clad fiber; GRIN, gradient index fiber; NCF, no core fiber.

With the complete system, we collected the spectra of 1) the probe in contact with the fingertip of a healthy volunteer and 2) 0.98 µM fluorescein for comparison. The probe was submerged in a dark water dump to measure the background emission. We compared impact of three emission filters on SBR performance of the catheter system (Table 1).

Table 1. Emission filter arrangement descriptions

Name	Description	Part Number	Vendor
Filter 1	485 Long pass emission filter	HQ485LP	Chroma Technology Corp, Vermont
Filter 2	510/84 Bandpass emission filter	FF01-510/84-25	Semrock, New York
Filter 3	525/70 Bandpass emission filter	ET525/70m-2pm	Chroma Technology Corp, Vermont

2.2. Power and spectral measurement system

Fluorescence power and spectra of fiber optics and optical components present in our OCT-AFI system were measured using the apparatus illustrated in Fig. 3. A 450 nm laser diode source (LP450-SF15, Thorlabs, New Jersey) was coupled into a low fluorescence optimized DCFC (CCP-09028, Castor Optics Inc., Canada). As the SMF between the source and DCFC is few-mode at 450 nm, we used a mode scrambler to reject overlaunched light. Excitation light was removed with a 485 long pass filter (Filter 1, HQ485LP, Chroma Technology Corp, Vermont) prior to detection using a pair of fiber collimators (F280FC-A, Thorlabs, New Jersey) fitted in a 60 mm cage cube (DFM2, Thorlabs, New Jersey). After filtering, the emission was directed into one of two detectors: spectra were measured using a 189-891 nm, 2048-pixel diffraction grating spectrometer (USB2000 + H04609, Ocean Optics, Florida); power was measured using a fiber-adapted meter (S150C, Thorlabs, New Jersey). Samples and the DCFC dump were terminated into a water dump contained in a 9 mL borosilicate test tube (9800-13, Corning, Arizona) wrapped in black absorptive foil (BKF12 Thorlabs, New Jersey). By wrapping the water dump with absorptive foil using, we intended to ensure that there would be no ambient or stray light collected by the bare fiber tip. Although measurements were collected in a dark room, this approach limited the opportunity for light escaping from the sample fiber or the laser display screen to impact our measurements. The DCFC dump (port R) could alternatively be polished to an angle exceeding the ability of the core and inner cladding to guide reflected light,

Biomedical Optics EXPRESS

eliminating the need of a water dump for image collection. Spectra were smoothed using the Matlab "lowess" model (local weighted linear least squares and 1st degree polynomial) across 40 points, to minimize noise while still showing small features [59]. SBR (Eq. (1)) was calculated and compared using the spectrometer measurements by,

$$\mathrm{SBR} = \frac{\sum_\lambda I_T(\lambda) - \sum_\lambda I_B(\lambda)}{\sum_\lambda I_B(\lambda)}, \tag{5}$$

where $I_T(\lambda)$ and $I_B(\lambda)$ represents the total and background spectrometer spectral intensity, respectively.

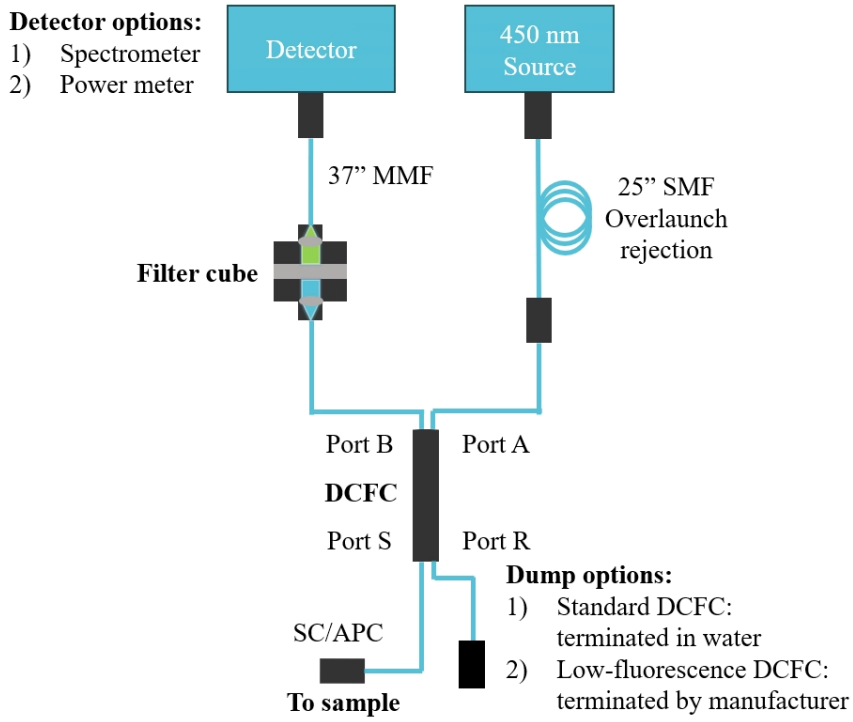

Fig. 3. Fluorescence measurement system schematic

The excitation light was deactivated between each measurement to mitigate photobleaching. Measurements of laser power over time showed a sharp peak when the laser was initialized, which settled within five seconds. Laser power decreased by ~5% over 30 minutes of continuous activation following an approximately exponential decay. However, repeated measurements of the DCFC fluorescence power at the beginning and end of each data collection session generated identical values. Each measurement taken allowed 30 seconds of settling time before collection to minimize this effect.

2.3. DCFC comparison

We explored two system configurations to compare the measured fluorescence power emission of a standard DCFC (DC1300LEFA, Thorlabs, New Jersey) against a specialized low-fluorescence version (CCP-09028, Castor Optics Inc., Canada). The low fluorescence DCFC includes several adjustments to reduce emission, including black hytrel furcation tubing, low-fluorescence epoxy, replacing DCF on Port A with SMF, replacing DCF on Ports B and R with MMF, and inclusion of dark termination at the dump on Port R. These adjustments have been demonstrated by Formozov

Biomedical Optics EXPRESS

et al. to improve fluorescence signal-to-noise ratio of a multimode circulator [60], which then were applied to produce the low-fluorescence DCFC. The filtered output fluorescence power and insertion losses at each port were also measured for each DCFC using a power meter (S120C and S150C, Thorlabs, New Jersey).

2.4. Optical fiber termination

We assessed performance of cleaved, scissor cut, and crushed fiber termination methods. The three methods represent differing topographic characteristics due to their fracture mechanisms. Higher topographic variation is expected to generate improved coupling due to low occurrence of angles capable of back-reflection. Minimized and repeatable detected power value is desirable, indicating high coupling of excitation blue light out the tip of the fiber. The power returning to the detector from a 2 m length of acrylate-coated DCF (SM-9/105/125-20A, Coherent, Pennsylvania) was measured in triplicate for each method. A hand cleaver (CT-30, Fujikura Ltd., Japan) was used for flat cleaved termination. Standard laboratory scissors were used for both the scissor cut and crushed tips termination. For scissor cut, the stripped end of the fiber was snipped with the sharp edge of the scissor perpendicular to the optical axis. For the crushed tips, the optical fiber was placed on a laboratory bench and force was applied perpendicular to the optical axis using the dull side of the scissor tip to the bare end of the fiber until failure. For each trial, we measured the unfiltered power with the sample tip exposed to air and submerged in water.

2.5. Optical fiber cutback

We quantified fluorescence contribution of optical fiber samples using a cut-back method: the fluorescence spectrum was measured using a 5 m sample of each fiber under blue light excitation (450 nm), spectral measurements were repeated after incrementally reducing fiber length by 1 m (in a manner similar to [61]) until 1 m remains. This generated five measurements for each 5 m sample of fiber examined. Fiber coatings and jacketing were stripped ~1 cm from the tip, scissor cut, then terminated in water to reject excitation light. All fibers were connectorized and polished with a rotating disk lapping machine to a 0.5 µm finish grit using the method described in [62]. The sample was connected to the spectrometer continuously throughout the experiment to avoid changes due to re-coupling. An integration time of 150 ms was used for all measurements, which was selected such that the highest emission sample utilized the entire dynamic range of the detector without saturation.

2.6. Signal model and calibration

The power of each sample was measured before the first and after the final spectra were collected. The result is a set of co-registered power and spectra at 1 m and 5 m for each fiber, which we used to calibrate the spectrometer measurement. Sample fluorescence power, in units of nanowatts,

$$F(\mathrm{L}) = L\alpha + \epsilon, \tag{6}$$

is approximated as a linear relationship where L is fiber length, α is per-meter fiber fluorescence (linear fluorescence efficiency), and ϵ is the error. To generate the desired linear relationship, spectrometer measurements were converted into power by integrating the intensity across wavelength and multiplied by a calibration coefficient. We then perform linear regression to extract α. The Matlab "fitlm" function [59] was used to calculate α, as well as the standard error of linear fluorescence efficiency slope, $SE_{\hat{\alpha}}$.We calculate the dark corrected intensity for each

Biomedical Optics EXPRESS

measurement, m, in arbitrary units,

$$R_m = \sum_{\lambda} (I_m(\lambda) - I_{\text{Dark}}(\lambda)), \tag{7}$$

where the dark spectral intensity without excitation is $I_{\text{Dark}}(\lambda)$, and the excited measured intensity is $I(\lambda)$. The estimated fluorescence power,

$$F_m = c\, R_m, \tag{8}$$

can then be calculated for sample lengths between 1 m and 5 m, where a corresponding power measurement is not available. A calibration parameter, $c = \frac{\sum_1^M \frac{P_m}{R_m}}{M}$, is applied, in units of nanowatts per arbitrary unit, where P_m is the power measured for measurement m, and M is the total number of measurements. This parameter represents the mean power per spectrometer unit based on all measured power and spectra pairs.

2.7. Collagen solidification

A 6240 uL batch of collagen I (Rat Tail Collagen I, 354236, Corning, Arizona) was aliquoted into units of 65 uL using a 96 well plate and crosslinked in an incubator at 37°C. It was diluted to a concentration of 1.7 mg/ml with Roswell Park Memorial Institute 1640 Medium (Thermo Fisher Scientific, Massachusetts). Solids were combined in a glass test tube, and deionized water was added for refractive index matching during measurement.

3. Results

3.1. Power and spectra measurement system characterization

Prior to data collection, we characterized the measurement system to determine spectrometer dark current (excitation source inactive) and system background fluorescence (excitation source active, without a sample). The aim of this experiment was to quantify fluorescence contribution of the system and identify differences in DCFC contribution. The low fluorescence DCFC has a fluorescence peak at ~670 nm, with total background emission 40% of the magnitude of the standard DCFC, which had a peak of ~650 nm (Fig. 4). A small part of the tail of the distribution is cut-off by the 485 long pass filter (Filter 1) as it approaches zero. To isolate the sample contribution, we subtracted the combined dark signal and component fluorescence from all other measurements presented (Eq. (7)).

The standard DCFC showed 1.6 dB of excitation light insertion losses measured at output of the sample arm (Port S, Fig. 3) compared to 0.2 dB in the low-fluorescence version (Table 2). There was a 41.6 dB vs. 45.9 dB reduction of the excitation light intensity at the detector (Port B). After filtering, the detected measurement system background fluorescence emission was 53.4 dB vs. 57 dB lower than the excitation power. As the low-fluorescence DCFC had lower background emission and higher throughput to the sample, it was selected to be used for all other measurements throughout this work.

3.2. Optical fiber termination

We then sought to evaluate the impact of fiber termination on back-reflections occurring at the sample tip. Scissor cut provides the lowest (61.7 nW) and most consistent average output power (coefficient of variation of 1.9) compared to cleaved (270 nW, coefficient of variation of 87.5) or crushed termination (65.7 nW, coefficient of variation of 6.8) (Table 3). As expected, all methods demonstrate higher detected power in air, compared to submerged in water due to index mismatch resulting in back-reflection of excitation light. Based on our data, we elected to terminate the fiber ends using scissor cut, due to the low and consistent level of back-reflected power returning

Biomedical Optics EXPRESS

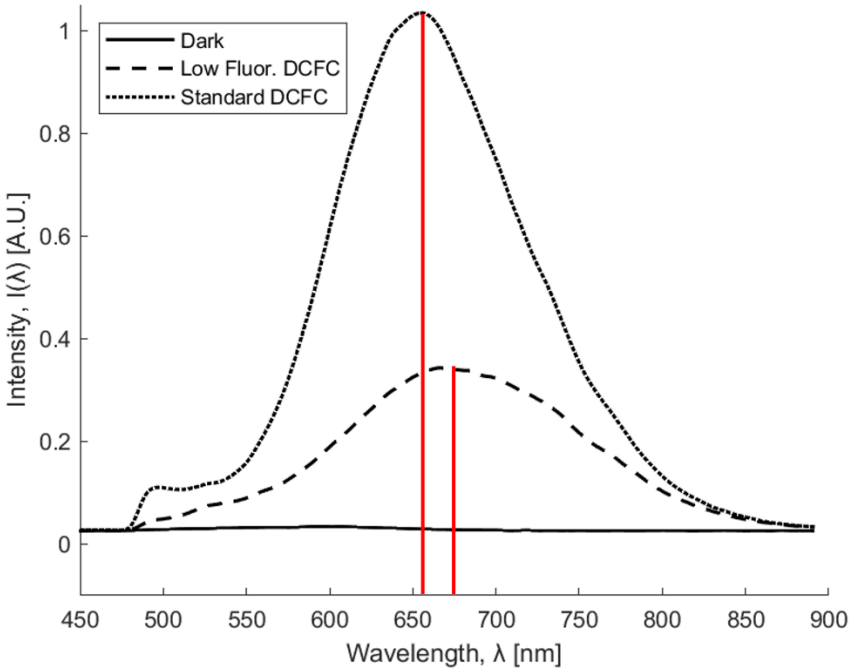

Fig. 4. Measurement system characterization, comparing fluorescence of the standard and low fluorescence DCFCs alongside the system noise. The low fluorescence DCFC is shown to have 40% of the background emission compared to the standard. The red line indicates the fluorescence peak for each spectrum.

Table 2. DCFC insertion losses and measurement system background fluorescence power

Location	Standard DCFC	Low-Fluorescence DCFC	Calibration Wavelength [nm]
Port A	1100 nW (0 dB)	1000 nW (0 dB)	450
Port S	750 nW (-1.6 dB)	950 nW (-0.2 dB)	450
Port B	0.075 nW (-41.6 dB)	0.026 nW (-45.9 dB)	450
Detector	0.005 nW (-53.4 dB)	0.002 nW (-57.0 dB)	650

to the detector. This reduces the amount of excitation light filtering required at the detector, as well as minimizing re-excitement of the sample on the return path. Cleaved and crushed termination methods show a large discrepancy between air and water output, suggesting high back-reflections occur at the air-glass interface. Crushed termination simultaneously achieves similar performance in water to that of scissor cut while also presenting high reflections in air.

Table 3. Optical fiber termination method comparison

Termination (n = 3 each)	Output Power in air (Mean ± SD) [nW]	Coefficient of Variation	Output Power in water (Mean ± SD) [nW]	Coefficient of Variation
Cleaved	3150 ± 3210	101.9	270 ± 236	87.5
Scissor Cut	400 ± 163	40.8	61.7 ± 1.2	1.9
Crushed	1166 ± 732	62.8	65.7 ± 4.5	6.8

Biomedical Optics EXPRESS

3.3. Optical fiber cutback

Combining the results of the experiments above, we then characterized the fluorescence properties of optical fibers while correcting for system background. We explored differing index of refraction profiles (SMF, MMF, DCF), coatings (polyimide, acrylate) and jacketing (0.9 mm Hytrel (FT900Y, Thorlabs, New Jersey), 3 mm polyvinyl chloride (PVC) (FT030 – various colors, Thorlabs, New Jersey)). Optical fibers were selected to have uniform core and cladding sizes across samples (or as close as was commercially available). Where appropriate for their index profile, all selected fibers were composed of a combination of: a 9 μm germanium doped single mode core, and/or a 105 μm pure silica multimode core/cladding, and/or a 125 μm fluorine doped outer-cladding (Fig. 1).

We observed a consistent reduction in fluorescence emission peak when measuring after each cutback (Fig. 5(a)). Germanium doped fibers emitted a peak at ~650 nm for both SMF and DCF fibers, while fibers high in hydroxyl (OH^-) such as the MMF emit a distinct peak at ~540 nm due to a difference in fluorescence behavior (Fig. 5 (b)). We found DCF linear fluorescence efficiency (Eq. (6)), $\hat{\alpha}_{DCF} \cong 0.5\ \frac{nW}{m*mW}$, to be an order of magnitude larger than that of SMF, $\hat{\alpha}_{SMF} \cong 0.05$, and MMF, $\hat{\alpha}_{MMF} \cong 0.01$, (Table 4). Measured emission power, F_m (Eq. (8)), arising from the linear fluorescence efficiency, α, for each index of refraction profile is displayed in Fig. 5(c)) for multimode index profiles and Fig. 5 (d)) for single mode profiles. As per the model described above (Eq. (6)), we expect fluorescence emission to be linearly proportional to length. After accounting for measurement system background, we anticipate zero intensity when there is no fluorescing fiber, thus we fit the linear regression to a model where the power axis begins at zero. We suspect the inconsistency of standard error across the samples is due in part to a variation in laser power over time. This could be corrected in future works by simultaneously measuring the laser and fluorescence powers, allowing for calibration of background and sample emissions to the excitation power at the time of measurement. MMF with 3 mm black and orange jacketing shows disproportionately high error compared to other fibers with similar α values. The furcation tube encloses the fiber within a plastic sheath which we suspect may be illuminated by stray light escaping the fiber and produce a small amount of fluorescence that is recaptured by the MMF. The amount generated and recaptured may vary with the position of the fiber within the sheath, which may be causing inconsistency in their measurement.

Table 4. Summary of optical fiber properties and per meter fluorescence power

Fiber	Manufacturer	Index Profile	Coating	Jacketing	$\hat{\alpha}\left(\frac{nW}{m*mW}\right)^a$	$SE_{\hat{\alpha}}$
SM-9/105/125-20A	COHERENT	DCF	Acrylate	None	0.48	0.018
DCF13	THORLABS	DCF	Acrylate	None	0.55	0.009
FG105LCA	THORLABS	MMF	Acrylate	None	<0.001	<0.001
FG105UCA	THORLABS	MMF	Acrylate	None	<0.001	<0.001
	THORLABS	MMF	Acrylate	3 mm Black	0.04	0.008
	THORLABS	MMF	Acrylate	3 mm Orange	0.03	0.012
	THORLABS	MMF	Acrylate	0.9 mm Yellow	0.01	0.002
FG100LEP	THORLABS	MMF	Polyimide	None	0.01	0.002
SM1550P	THORLABS	SMF	Polyimide	None	0.13	0.004
SM1550P	THORLABS	SMF	Polyimide	0.9 mm Yellow	0.02	0.004
SMF130V	OMNILIT	SMF	Acrylate	None	0.02	0.003
SMF28J9	THORLABS	SMF	Acrylate	0.9 mm Yellow	0.07	0.001

[a]Linear fluorescence efficiency is reported in nW of measured fluorescence per meter of fiber per mW at 450 nm excitation

Biomedical Optics EXPRESS

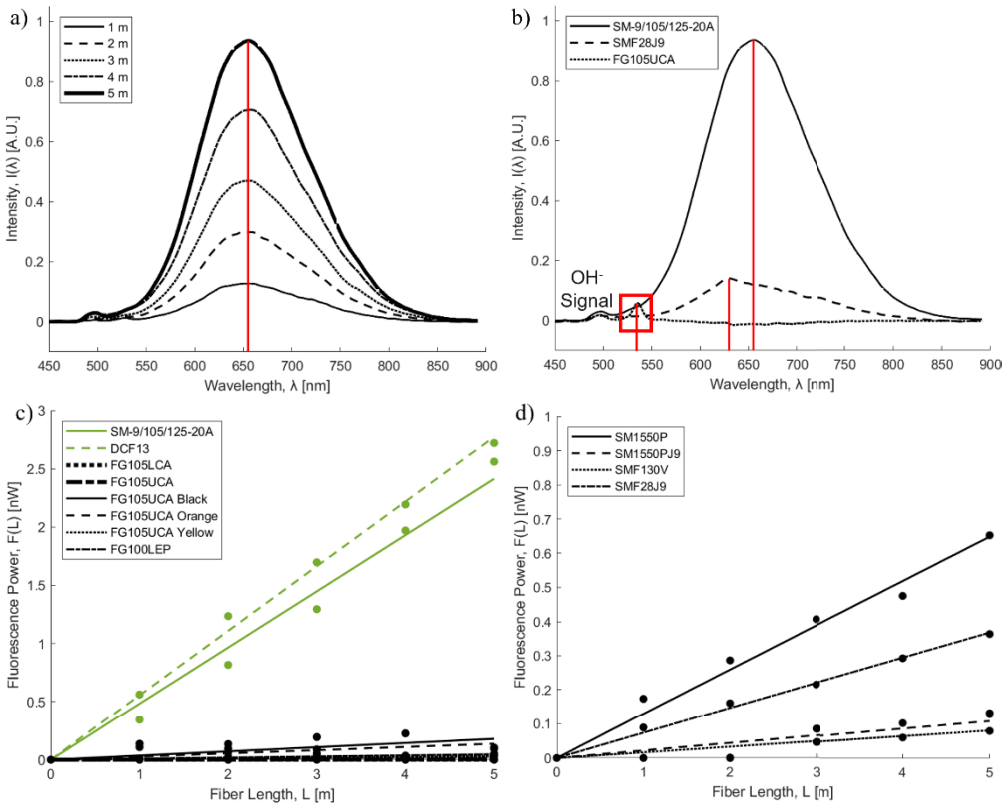

Fig. 5. a) Spectra gathered from 5 m DCF cutback experiment b) Spectra gathered from 5 m lengths of SMF, MMF, and DCF index profiles. The MMF visualized has high concentration of hydroxyl, which generates an additional peak at ~540 nm, which is indicated. c) Per-meter cutback fluorescence summary – MMF and DCF profiles d) Per-meter cutback fluorescence summary – SMF profiles. Details of each fiber number are described in Table 4.

3.4. *Tissue measurements*

Having established the fluorescence behavior of the optical fiber, we then explored the relative power and wavelength spectral distribution of interest for assessing structural proteins *in vivo*. We measured and compared the fluorescence spectra of crosslinked collagen I and fingertip tissue of five healthy volunteers. Fluorescence emission was collected using the scissor cut bare tip of a 2 m DCF fiber sample. The tip of the DCF fiber was placed against the solidified collagen and a fluorescence spectrum collected. We also placed the tip of the bare DCF fiber in contact with the fingertip of a healthy human volunteer and collected the generated fluorescence spectrum. For this measurement, the volunteers pinched the tip of the fiber between their fingertips, which we found to provide the most consistent response. The contribution of the 2 m DCF fiber was included in the subtraction of background fluorescence for these samples to isolate the contribution of the target. Background was measured and subtracted from each patient measurement set individually. The spectra of the collagen 1 and tissue targets were nearly identical with a peak at ~525 nm (Fig. 6(a)). Measurements of collagen 1 were taken with a higher integration time (500 ms) than the fingertips (150 ms) due to low intensity. Three measurements were collected from each volunteer. We observed large intensity variation between measurements of the same target but consistent spectral shape, indicating that background subtraction and filtering is an effective method to isolate the target signal. The tissue fluorescence peak is well separated from

Biomedical Optics EXPRESS

background, allowing for clear resolution of the tissue response after background subtraction (Fig. 6 (b)). Volunteers 1, and 2 were of Caucasian descent; volunteers 3, 4, and 5 were of West Asian descent. Differences in proteins and morphology have been previously demonstrated between ethnic skin types, which may explain differences in intensity [63]. Non-crosslinked collagen was found to be non-fluorescent with this excitation wavelength.

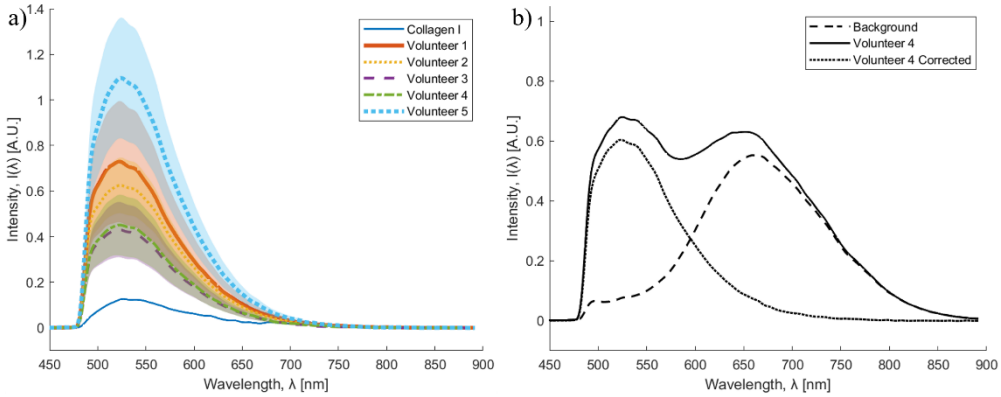

Fig. 6. a) Spectral comparison of cross-linked rat tail collagen I to *in vivo* human fingertip tissue of five healthy volunteers, demonstrating nearly identical spectra between the two targets. Shaded region indicates standard deviation calculated from three measurements. b) Volunteer fingertip spectra with background, before and after subtraction.

3.5. *Imaging system optimization*

Finally, we measured the per-component contribution of the catheter system (Fig. 2) and assessed improvements to SBR and image quality gained from practical implementation of this work. We quantified the magnitude of signal-to-background improvement from two changes: 1) replacing a standard DCFC with a low fluorescence optimized version (as described above), and 2) replacing the long pass filter used to remove excitation light with a bandpass filter to additionally reduce system fluorescence while passing target emission. The fluorescence spectra were measured as each component was added in sequence. As the detector is connected to Port B of the DCFC, the WDM and DCFC were examined as a unit and the same WDM was used for both DCFCs characterized.

All system components displayed a similar fluorescence peak of ~660 nm, the WDM and low-fluorescence DCFC contributes the largest portion (43%), followed by the FORJ (32%), and finally the catheter (26%) (Fig. 7). Percentage contributions of each component were calculated by subtracting the contribution of those upstream. We also note that systems consisting primarily of fibers with high OH^- content will produce fluorescence spectra overlapping with that of the tissue measurements presented above, which would make signal isolation challenging if using physical filtering in that configuration. Measuring the spectra of the catheter pressed against the fingertip tissue of a healthy human volunteer (Volunteer 1) produced an SBR of 0.63, compared to a SBR of 1.41 when submerged in 0.98 µM fluorescein (Eq. (5)).

The cut-off wavelength was selected to isolate the target fluorescence from that of the optical components. We used the inflection point visible at ~570 nm in the Fig. 7 "Catheter on Finger" measurement as a reference to identify the separation between target and background spectra. The catheter of the OCT-AFI system was submerged in 0.98 µM fluorescein solution and the spectra measured with and without the inclusion of the bandpass filter (Filter 2) to assess its impact (Fig. 8 (a)). The OD of the two filters as a function of wavelength are visualized in (Fig. 8(b)) [64,65]. We observed a reduction of the background fluorescence from 43% of the total signal

Biomedical Optics EXPRESS

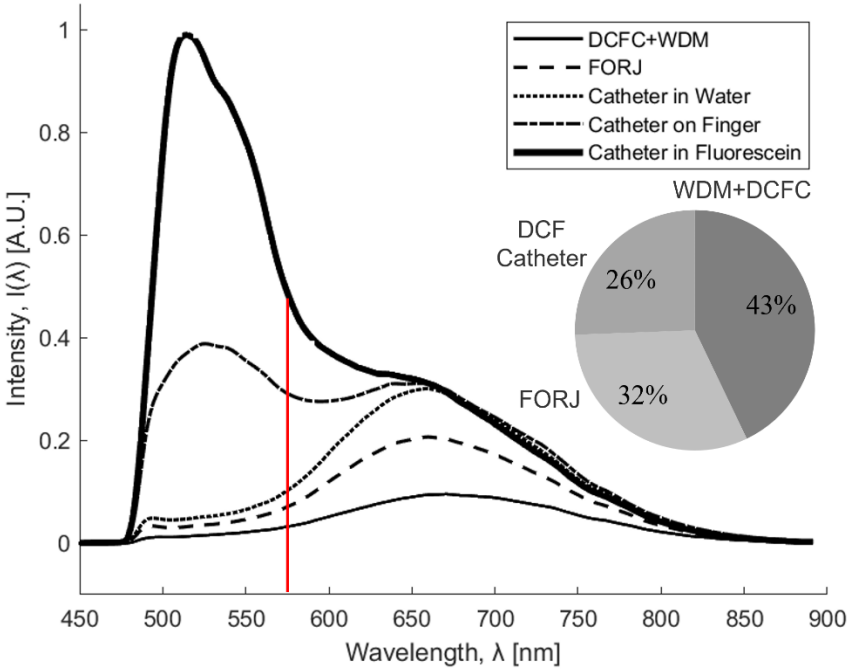

Fig. 7. Component fluorescence contribution spectra with a 485 nm long pass filter (Filter 1). The red line indicates an inflection point where the spectral intensity shifts from signal-dominated to background-dominated.

with the long pass filter (Filter 1) alone to 6% when including the bandpass (Filter 2) Fig. 8(c)). Excitation light was still detectable after filtering when using the 510/84 bandpass (Filter 2) without combining with the 485 long pass (Filter 1), perhaps due to a long spectral excitation tail or wavelength broadening within the system [66]. A bandpass filter (Filter 3) with a higher cut-off wavelength (490 nm vs. 468 nm) was selected for implementation in our clinical OCT-AFI cart to correct this issue. The cut-on wavelength was selected to fully block excitation light from reaching the spectrometer while maximizing signal throughput. After installing the updated bandpass filter (Fitler 3), SBR (Eq. (5)) increased from 1.24 to 10.7, and further increased to 13 after installing the low-fluorescence DCFC while measuring the fluorescein solution (Fig. 8 (d)).

Images were collected from Volunteer 1, comparing the original system with long pass filter (Filter 1) and standard DCFC (0.24 SBR Fig. 8(d); Fig. 9(a) and (b)) against the updated system with bandpass filter (Filter 3) and low-fluorescence DCFC (2.5 SBR Fig. 8(d); Fig. 9(c) and (d)). All images are collected with the same laser driving current and detector gain. Overall intensity is reduced in bandpass filtered images compared to the long-pass, indicating reduced background emission (Fig. 9(a) and (c)). To show usage of the detector range, the black level of these images is set to the zero of the detector range, while the white level is auto-contrasted to the 99th percentile of intensity. We observe reduced noise on the image and improved contrast of subtle features, such as sweat glands, which can be better identified with the optimized system (Fig. 9(b) and (d)). The black level was changed to the 0.1 percentile of intensity for this image pair, to show scaled image contrast.

Using the same configuration, we imaged fingertips while periodically removing contact with the catheter to examine contrast between air and signal (Fig. 10(a) and (c)). No scaling is applied to the images to demonstrate the fluorescence intensity magnitude collected from the two filter arrangements at the same detector gain. Histograms (Fig. 10(b) and (d)) show the intensity

Biomedical Optics EXPRESS

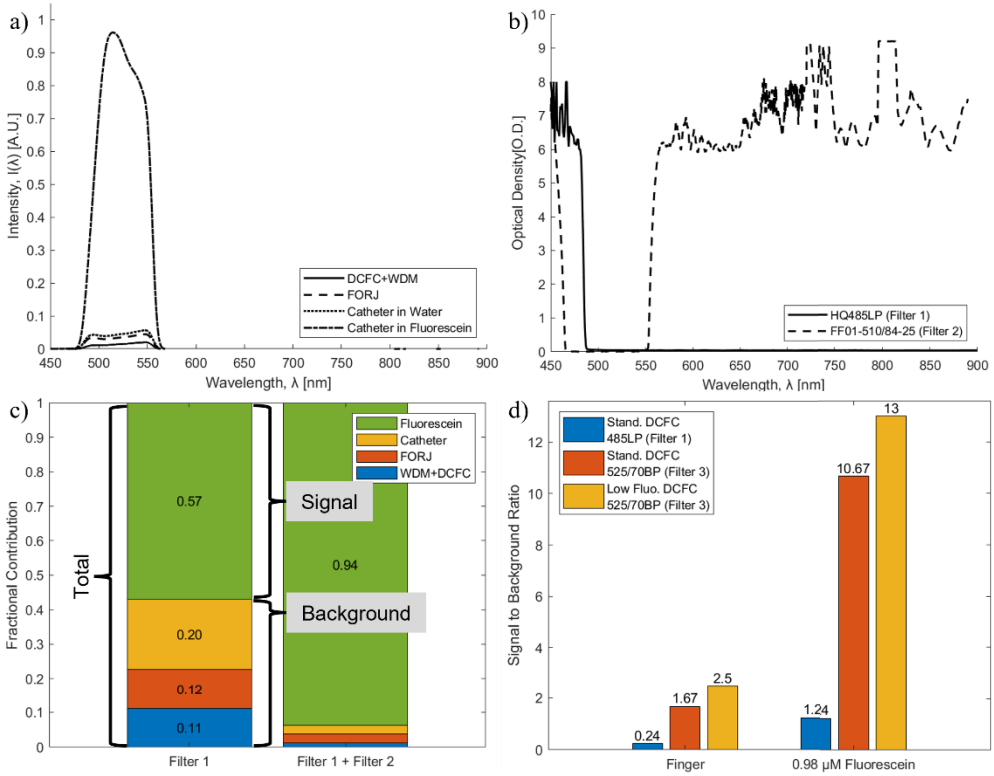

Fig. 8. Component fluorescence spectra with inclusion of a 485 nm long pass filter (Filter 1) in series with a 510/84 nm bandpass filter (Filter 2). a) Amplitude of the fluorescence spectra from the optical components. b) Optical density of the filters. c) SBR comparison, showing the fluorescein imaging target to have the largest portion of the total intensity, followed by the catheter, then the FORJ, and finally the WDM + DCFC. d) Fingertip and 0.98 μM fluorescein SBR comparison. Combinations of standard vs. low fluorescence DCFC and 485 nm long pass (Filter 1) vs. 525/70 nm bandpass (Filter 3) filters are explored. The low fluorescence DCFC with bandpass (Filter 3) is shown to have the highest SBR, followed by the standard DCFC with bandpass (Filter 3), then the standard DCFC with long pass (Filter 1) for both imaging targets.

distribution of pixels within the red boxes from their corresponding images, demonstrating improved SBR and contrast at the cost of intensity throughput. We fit Gaussian distributions to the air and tissue peaks of each filter arrangement, which shows a reduction in background (air) FWHM from 3.88 to 1.64 units of detector response (Table 5). This shows that the system background peak (air) is sharper and more isolated from the tissue fluorescence. Values lying between the two peaks originate from the edges of the fingertips in poor contact with the catheter, as well as a portion of the background. With a tightening of the background FWHM by switching from the long pass (Filter 1) to bandpass (Filter 3), more of the background can be rejected to reveal additional gray values of desired tissue fluorescence.

Representative images of human fingertips were also collected from all five volunteers to compare SBR acquired through the long pass (Fig. 11 (a), (c), (e), (g), (i)) and bandpass filters (Fig. 11(b), (d), (f), (h), (j)). All images were collected using the low-fluorescence DCFC, detector gain was adjusted to eliminate detector saturation and maintain similar sensing range utilization. Each volunteer was imaged once with each filter configuration, while periodically

Biomedical Optics EXPRESS

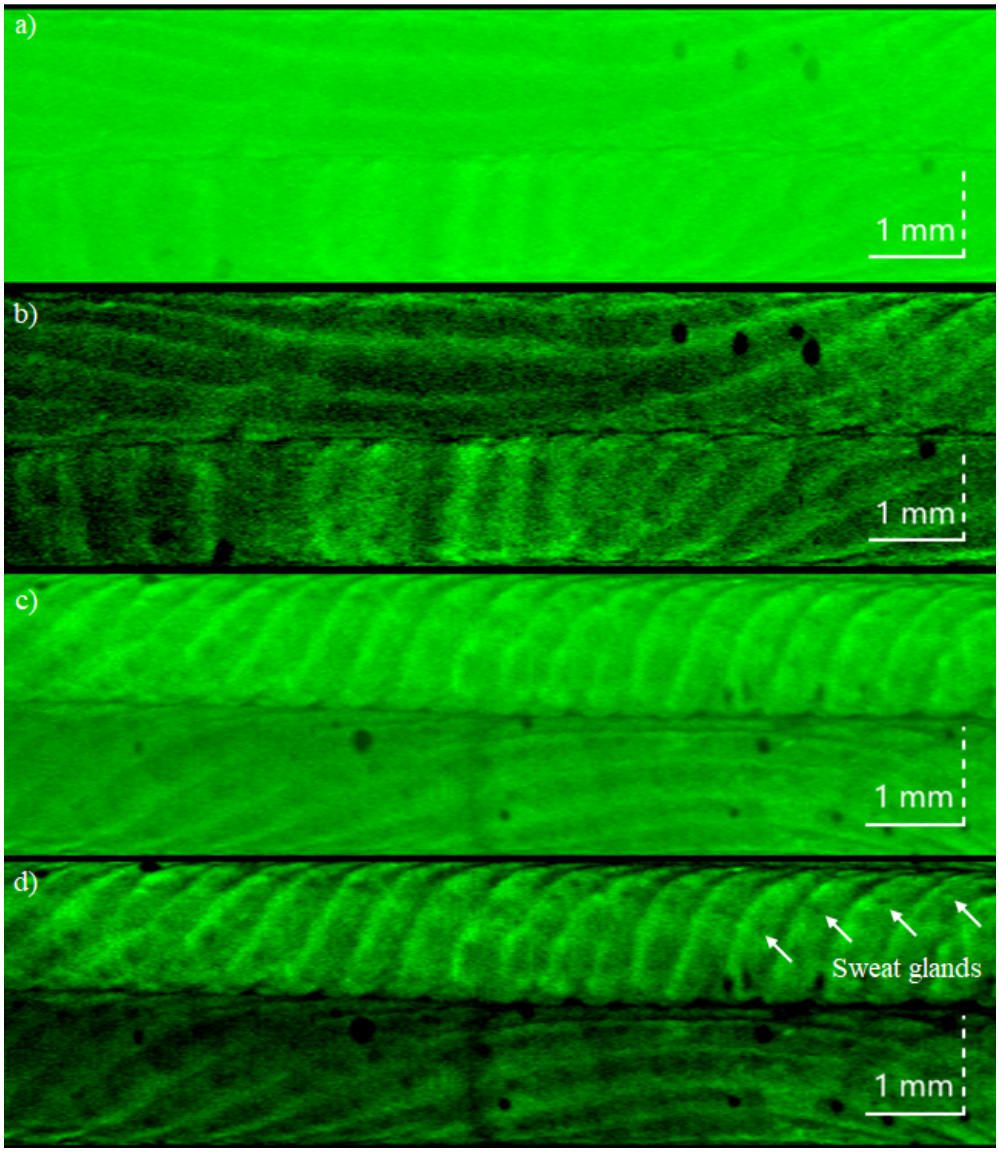

Fig. 9. Comparison of a, b) long-pass (485 nm cutoff, Filter 1) and c, d) bandpass (525/70 nm, Filter 3) filters for fluorescence imaging of human fingertip using a rotary pullback OCT-AFI catheter. a, c) Black level is set to the zero of the detector range, white level is auto-contrasted to the 99th percentile of intensity. b, d) Black level is auto-contrasted to the 0.1 percentile of intensity, white level is auto-contrasted to the 99th percentile of intensity. Improvements in noise and subtle feature discrimination are apparent. Sweat glands (white arrows) become clearly discernable using the bandpass filter, that were not previously easily observed. Overall intensity is reduced in bandpass filter images compared to the long-pass, indicating reduced background emission. All images are collected using the same laser driving current and detector gain.

Biomedical Optics EXPRESS

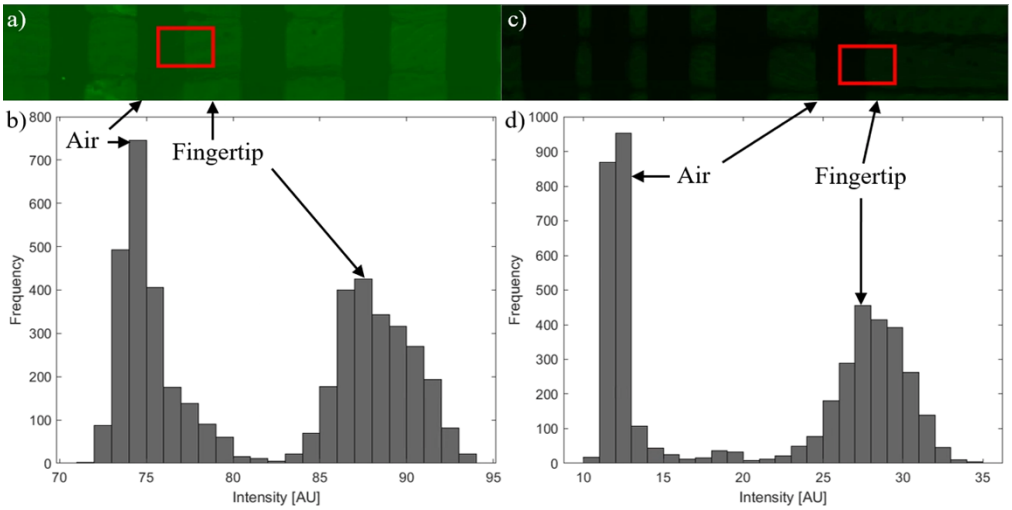

Fig. 10. Comparison of a, b) long-pass (485 nm cutoff, Filter 1) and c, d) bandpass (525/70 nm, Filter 3) filters for fluorescence imaging of human fingertip using a rotary pullback OCT-AFI catheter. Images depict fingertips with periodical removal of contact with the catheter to examine the contrast between air and signal; they are taken at the same detector gain with no scaling applied. Histograms b) and d) show the intensity distribution of pixels within the red boxes from their corresponding images.

Table 5. Gaussian fitting parameters of histograms shown in Fig. 10(b) and (d)

Filter	Medium	Peak [AU]	FWHM [AU]
Long pass (Filter 1)	Air	74.6	3.88
	Tissue	87.9	5.13
Bandpass (Filter 3)	Air	11.6	1.64
	Tissue	27.3	6.72

removing contact. The black and white levels were auto-contrasted to the 0.1 percentile and 99th percentile of intensity, respectively. SBR was calculated (Eq. (1)) for each image by averaging the contrast between three air-tissue contact iterations. The long pass filtered images had an average SBR of 0.085 with a standard deviation of 0.016, while the bandpass filtered images had an average SBR of 0.66 with a standard deviation of 0.25. SBRs measured here are lower than those of Fig. 9 and Fig. 10 as a less sensitive catheter was used for image acquisition. Further, improvements from replacing the DCFC with the low-fluorescence version are included in both filter measurements. There was an average SBR improvement of 7.9x (2.9 standard deviation) after implementation of the bandpass filter across all images. The mean of the bandpass filtered images differed from that of the long pass images with a statistical significance of $p = 0.001$ using a paired two-tailed student's t-test [67].

4. Discussion

We present characterization of optical fiber autofluorescence under 450 nm excitation and explore the ramifications on imaging system design. We identified a 2.5x difference in background fluorescence emission between a standard and low fluorescence optimized DCFC (Fig. 2). Through cutback experiments of a variety of optical fibers, we have shown that DCF delivers an order of magnitude greater background fluorescence (~0.5 nW/m/mW) compared to SMF

Biomedical Optics EXPRESS

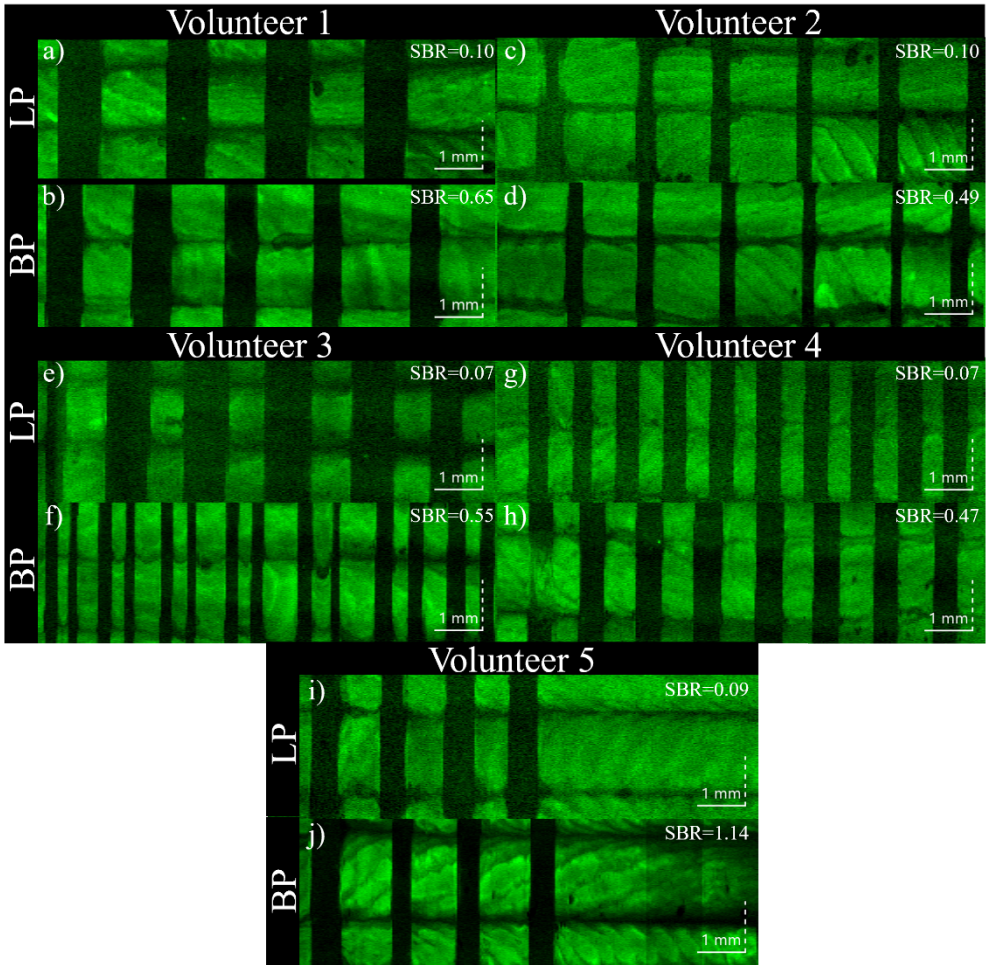

Fig. 11. Fingertip autofluorescence imaging comparison from five volunteers, comparing SBR of long pass filter (LP, 485 nm cutoff, Filter 1) to bandpass filter (BP, 525/70 nm, Filter 3). Black level is auto-contrasted to the 0.1 percentile of intensity, white level is auto-contrasted to the 99th percentile of intensity. SBR is calculated between air and tissue utilizing periodic removal of contact.

(~0.05), MMF (~0.01) (Table 4). Connector epoxies were found to have minimal effect on fluorescence intensity and spectra of the samples tested. We observed that optical fibers generally emit with a peak wavelength of approximately 660 nm under 450 nm excitation (Fig. 5). We found there is a linear relationship between fluorescence intensity and fiber length, which varies with the refractive index profile. We measured an emission peak of ~525 nm from collagen I, which matched the spectral shape collected from the fingertips of five healthy volunteers (Fig. 6 (b)). We demonstrated the implementation of these findings through an average 7.9x improvement in measured SBR when using a 525/70 nm bandpass filter (Filter 3) compared to a 485 nm long pass filter (Filter 1) (Fig. 8 (c)). Based on our results, this band rejects the majority of system background fluorescence arising from fiber optic components, while passing collagen-based tissue fluorescence.

We show that the collection and back-propagation of fluorescence from dopants in the fiber core is a significant mechanism for the generation of background fluorescence in fiber optic

Biomedical Optics EXPRESS

systems. The amount of background collected is linearly proportional to the length of fiber excited and varies depending on the dopant type and concentration, as well as the NA of the fiber. Fiber collection factor is proportional to NA squared for both system background and tissue. We expect to see changes at the same rate with increasing fiber NA. Although separation of excitation and collection paths may address collection of dopant fluorescence, it is not feasible for imaging in small-diameter organ applications. Therefore, SBR and image quality must be addressed through filtering or processing, rather than increasing collection.

Based on the findings of this work, we have identified the following approaches to optimize a system for autofluorescence imaging. Wherever possible, lengths of fiber with doping present in the core should be minimized or eliminated from the excitation path. A bandpass filter should be utilized, targeted to both remove excitation light that is scattered into the detection path and isolate the desired emission band from the system background. Alternatively, if real-time imaging were not necessary for the application, data collection using a spectrometer would allow for computational restriction of the collected emissions to select for the target spectra to achieve a similar gain in SBR. Use of a single-photodetector arrangement enables measurement of far smaller intensities than that of a spectrometer, which is necessary for high acquisition speeds. Where available, low-fluorescence components should be used – particularly for the DCFC and FORJ. Fibers and connectors should be selected to minimize optical core misalignment. Finally, if the DCFC dump is not terminated by the manufacturer, the bare fiber tip should be scissor cut and terminated in water to minimize back-reflections.

Based on our modeling of autofluorescence coupling, we expect 2x greater background fluorescence collection (0.17% vs. 0.31%) in DCF compared to SMF fibers. This would assume complete coupling of all collected fluorescence in the SMF core to the cladding of the DCFC which is then directed to the detector without losses. Our experimental data shows ~5x greater DCF fluorescence. This suggests that there was only partial coupling of the collected fluorescence from the SMF core into the cladding of the DCFC. As the MMF we examined have pure silica cores, we expect them to generate very little fluorescence. However, they may collect and propagate fluorescence coupled into them from other sources (such as the SMF leading from the source, or the DCFC) resulting in greater fluorescence than expected.

Xiang et al. present a spectral unmixing algorithmic approach to address the issue of system background fluorescence in single-fiber imaging systems [55]. They deploy 785 nm excitation, with the goal of isolating indocyanine green (ICG) from system autofluorescence. The optical path is similar to the one presented here, utilizing a DCFC, FORJ, and DCF-based catheter. Through post-processing using spectral unmixing, they identify and eliminate system fluorescence that overlaps with their desired target spectra. This approach necessitates use of a spectrometer for fluorescence detection, rather than a photomultiplier tube or avalanche photodiode, limiting image acquisition speed. They present measurements of system fluorescence with and without an excitation bandpass filter, demonstrating results in concordance with our observations that excitation light can leak and contribute background. Per-component fluorescence contribution ratios appear to be similar to our observations. Interestingly, they observe a 45% reduction in background by reducing the fiber length between the DCFC and FORJ. As DCF is used for this length, this aligns with our results, indicating this reduction is likely due to lower generation of fluorescence by excitation light traveling along this shorter fiber. Using phantom and *in vivo* imaging, they show successful removal of system background fluorescence arising from sharp reflection interfaces. We propose a hardware-based approach to accomplish the same goal of system fluorescence mitigation. Our method permits real-time collection and display of data but is unable to differentiate target from system fluorescence in the case of overlapping spectra. Xiang's approach, although requiring post-processing and slower acquisition, addresses the concern of overlapping spectra. The findings of these two approaches are synergistic with one another, allowing for implementation of both simultaneously.

Biomedical Optics EXPRESS

We observed that fibers with pure silica cores generated negligible autofluorescence compared to those with doped cores; germanium doping is used in standard single mode fiber cores, which causes much more fluoresce than pure silica cores in multimode fibers with fluorine doped claddings (Table 4). The DCFs we explored consist of a germanium doped core, a pure silica inner-cladding, surrounded by a fluorine doped second cladding; this results in high fluorescence excitation of the core on the forward path, which is then collected by the second cladding and returned to the detector (Fig. 1). Fluorescence in silica with a center wavelength of ~650 nm has been previously identified to be a result of non-bridging oxygen hole center defects [68,69]. Our measurements, as well as those by Johansson et al., demonstrate fluorescence peaks coinciding with the presence of these defects [57]. It has been shown that this fluorescence peak is generated due to heat treatment of fused silica in the presence of H_2 [70,71]. There is an opportunity to explore untreated fabrication methods to reduce fluorescence in commercial optical fibers.

We suspect that fiber misalignment resulting from manufacturing and assembly tolerances result in power being coupled from the SMF core into the cladding of the DCF, thus allowing the SMF emission to reach the detector. Although SMF fluorescence is not consistently measurable due to this variability, it is included as demonstration of this effect. SMF fluorescence should be considered, even if only to minimize background emission from the excitation source.

Most fiber fluorescence generated in the core is not initially captured by the inner-cladding, however reflections at the fiber surface present an opportunity for additional coupling. We observed that polyimide-coated SMFs have higher measured fluorescence than those coated in acrylate. This is not recreated in the MMF samples, which have very little fluorescence, in both acrylate and polyimide coatings. Therefore, we suspect that differences in refractive index between acrylate (typically 1.4–1.6) and polyimide (1.6–1.8) [72] relative to glass may cause greater reflections in polyimide, allowing more emitted fluorescence to be recollected by the fiber and delivered to the detector. However, testing of additional samples would be required to separate this from the variability of core-cladding alignment due to tolerance stack-up.

We observed a large spectral peak just above the filter cutoff (485 nm) in some fiber samples. We were able to replicate this behavior by comparing the spectrometer measurement of the DCFC with nothing connected (terminated in air), directing the output toward a mirror. This suggests that the behavior is caused by a bright reflection of the excitation light being coupled into the sample arm; we hypothesize that over-polished connectors introduce an air gap at the interface resulting in a reflection cavity that generates this artifact.

This study is limited by use of a single excitation wavelength. Based on the results of Udovich et al. [45] we expect that wavelengths closer to 350 nm will result in higher fluorescence intensity per meter of fiber. At longer wavelengths, such as at 785 nm explored by Xiang et al. [55], we expect lower fiber fluorescence intensity. The methods we present would be viable at other wavelengths, as one may be able to selectively remove background using a different appropriately tailored bandpass filter. Measurements of the FORJ fluorescence in this work are limited to Princetel devices that contain the same quantity and type of fluid within the optical path. In future work, a sample of this fluid could be requested from the vendor and its fluorescence behavior characterized to assess impact on the system. Alternatively, glycerol could be used as an index matching fluid in a custom FORJ, which exhibits very low fluorescence at 450 nm. Use of a FORJ can also be avoided altogether through implementation of micromotor actuation [73,74], which has previously been demonstrated for multimodal applications [75]; this is an ideal platform for translation of the work presented here. We did not account for sensor variation with wavelength or nonlinearity. Laser power output was not continuously measured, so we cannot account for variations in power co-registered to fluorescence measurements. Additional limitations include that we assume uniform doping and material properties throughout the fiber length. We also assume all fibers with the same core/cladding geometry and index profile have the same dopants and material properties. We measured one replicate for each fiber, with five

Biomedical Optics EXPRESS

cutback measurements. Through linear regression, we produce a robust measurement of linear fluorescence efficiency of that single sample. However, this does not account for inter-sample variability due to manufacturing tolerances. Dopant concentrations may vary across fiber pulls, but we expect negligible difference from samples collected at the same section of the reel. Variation between batches of the same fiber are expected to be small relative to different refractive index profile designs. Impacts of photobleaching are not considered. Future work will address implementing the suggested changes from this work for clinical study, where we will measure healthy and dysplastic tissue within human luminal organs.

5. Conclusion

We have characterized the fluorescence power emission and spectra of optical fibers and an OCT-AFI system for optimization of performance under 450 nm excitation. We performed cutback experiments on a selection of optical fibers to identify the strongest contributing factors to fiber background fluorescence. We characterized the fluorescence emission from the components of an OCT-AFI system, as well as that of collagenous tissue targets. We demonstrated an average 7.9x improvement in signal to background ratio while imaging with the system by including a bandpass filter to reduce system fluorescence reaching the detector. The results of this study can be used to improve the fluorescence performance of OCT-AFI systems that utilize 450 nm excitation.

Funding. Canadian Institutes of Health Research (178381, 203697); Natural Sciences and Engineering Research Council of Canada (RGPIN-2023-05592); Mitacs (Accelerate).

Acknowledgements. Thank you to Alicia Fung for assistance in preparation of optical fiber samples and Ian Wang for assistance in data collection.

Disclosures. The authors declare no conflicts of interest.

Data availability. Data underlying the results presented in this paper are available by request to the corresponding author.

References

1. M. Monici, "Cell and tissue autofluorescence research and diagnostic applications," Biotechnology Annual Review **11**, 227–256 (2005).
2. L.-M. W. K. Song, S. Banerjee, D. Desilets, *et al.*, "Autofluorescence imaging," Gastrointestinal Endoscopy **73**(4), 647–650 (2011).
3. C. Schönmann and K. Brockow, "Adverse reactions during procedures: Hypersensitivity to contrast agents and dyes," Annals of Allergy, Asthma & Immunology **124**(2), 156–164 (2020).
4. Y. Jiao, Y. Liu, and M. Jin, "Exploring the dark side of diagnostic dyes with a focus on Indocyanine green's adverse reactions," Sci. Rep. **14**(1), 30155 (2024).
5. I. S. Kornblau and J. F. El-Annan, "Adverse reactions to fluorescein angiography: A comprehensive review of the literature," Surv. Ophthalmol. **64**(5), 679–693 (2019).
6. J. Meira, M. L. Marques, F. Falcão-Reis, *et al.*, "Immediate Reactions to Fluorescein and Indocyanine Green in Retinal Angiography: Review of Literature and Proposal for Patient's Evaluation," Clin Ophthalmol. **14**, 171–178 (2020).
7. R. George, M. Michaelides, M. A. Brewer, *et al.*, "Parallel factor analysis of ovarian autofluorescence as a cancer diagnostic," Lasers Surg. Med. **44**(4), 282–295 (2012).
8. M. A. Brewer, U. Utzinger, J. K. Barton, *et al.*, "Imaging of the Ovary," Technology in Cancer Research & Treatment **3**, 617 (2004).
9. M. Zellweger, P. Grosjean, D. Goujon, *et al.*, "In vivo autofluorescence spectroscopy of human bronchial tissue to optimize the detection and imaging of early cancers," J. Biomed. Opt. **6**(1), 41–51 (2001).
10. D. J. Anthony, A. E. Profio, and O. J. Balchum, "Fluorescence Spectra in Lung with Porphyrin Injection," Photochem. Photobiol. **49**(5), 583–586 (1989).
11. B. Palcic, S. Lam, J. Hung, *et al.*, "Detection and localization of early lung cancer by imaging techniques," Chest **99**(3), 742–743 (1991).
12. Ts. Genova, H. Valkov, B. Vladimirov, *et al.*, "Endogenous and exogenous fluorescence diagnosis of tumors in the lower part of the gastrointestinal tract," J. Phys.: Conf. Ser. **1859**(1), 012039 (2021).
13. A. Gillenwater, R. Jacob, R. Ganeshappa, *et al.*, "Noninvasive Diagnosis of Oral Neoplasia Based on Fluorescence Spectroscopy and Native Tissue Autofluorescence," Arch. Otolaryngol. Head Neck Surg. **124**(11), 1251–1258 (1998).

Biomedical Optics EXPRESS

14. C. S. Betz, H. Stepp, P. Janda, *et al.*, "A comparative study of normal inspection, autofluorescence and 5-ALA-induced PPIX fluorescence for oral cancer diagnosis," Int. J. Cancer **97**(2), 245–252 (2002).
15. I. Pavlova, M. Williams, A. El-Naggar, *et al.*, "Understanding the Biological Basis of Autofluorescence Imaging for Oral Cancer Detection: High-Resolution Fluorescence Microscopy in Viable Tissue," Clin. Cancer Res. **14**(8), 2396–2404 (2008).
16. J. Hung, S. Lam, J. C. Leriche, *et al.*, "Autofluorescence of normal and malignant bronchial tissue," Lasers Surg. Med. **11**(2), 99–105 (1991).
17. S. Lam, T. Kennedy, M. Unger, *et al.*, "Localization of Bronchial Intraepithelial Neoplastic Lesions by Fluorescence Bronchoscopy," Chest **113**(3), 696–702 (1998).
18. T. C. Kennedy, S. Lam, and F. R. Hirsch, "Review of Recent Advances in Fluorescence Bronchoscopy in Early Localization of Central Airway Lung Cancer," The Oncologist **6**(3), 257–262 (2001).
19. H. Weingandt, H. Stepp, R. Baumgartner, *et al.*, "Autofluorescence spectroscopy for the diagnosis of cervical intraepithelial neoplasia," BJOG: An International Journal of Obstetrics & Gynaecology **109**(8), 947–951 (2002).
20. R. Drezek, C. Brookner, I. Pavlova, *et al.*, "Autofluorescence Microscopy of Fresh Cervical-Tissue Sections Reveals Alterations in Tissue Biochemistry with Dysplasia," Photochem. Photobiol. **73**(6), 636–641 (2001).
21. M. A. Kara and J. J. G. H. M. Bergman, "Autofluorescence Imaging and Narrow-Band Imaging for the Detection of Early Neoplasia in Patients with Barrett's Esophagus," Endoscopy **38**(6), 627–631 (2006).
22. B. Mayinger, P. Horner, M. Jordan, *et al.*, "Light-induced autofluorescence spectroscopy for the endoscopic detection of esophageal cancer," Gastrointestinal Endoscopy **54**(2), 195–201 (2001).
23. P. M. Lane, T. Gilhuly, P. Whitehead, *et al.*, "Simple device for the direct visualization of oral-cavity tissue fluorescence," J. Biomed. Opt. **11**(2), 024006 (2006).
24. D. Shin, N. Vigneswaran, A. Gillenwater, *et al.*, "Advances in fluorescence imaging techniques to detect oral cancer and its precursors," Future Oncol. **6**(7), 1143–1154 (2010).
25. T. D. Wang, J. M. Crawford, M. S. Feld, *et al.*, "In vivo identification of colonic dysplasia using fluorescence endoscopic imaging," Gastrointestinal Endoscopy **49**(4), 447–455 (1999).
26. D. Hanahan and R. A. Weinberg, "Hallmarks of Cancer: The Next Generation," Cell **144**(5), 646–674 (2011).
27. K. Song, Z. Yu, X. Zu, *et al.*, "Collagen Remodeling along Cancer Progression Providing a Novel Opportunity for Cancer Diagnosis and Treatment," Int. J. Mol. Sci. **23**(18), 10509 (2022).
28. D. Hanahan, "Hallmarks of cancer—Then and now, and beyond," Cell **189**(8), 2254–2277 (2026).
29. S. Lam, C. MacAulay, J. Hung, *et al.*, "Detection of dysplasia and carcinoma in situ with a lung imaging fluorescence endoscope device," The Journal of Thoracic and Cardiovascular Surgery **105**(6), 1035–1040 (1993).
30. N. Vigneswaran, S. Koh, and A. Gillenwater, "Incidental detection of an occult oral malignancy with autofluorescence imaging: a case report," Head Neck Oncol. **1**(1), 37 (2009).
31. F. P. Koch, P. W. Kaemmerer, S. Biesterfeld, *et al.*, "Effectiveness of autofluorescence to identify suspicious oral lesions—a prospective, blinded clinical trial," Clin. Oral. Invest. **15**(6), 975–982 (2011).
32. C. F. Poh, S. P. Ng, P. M. Williams, *et al.*, "Direct fluorescence visualization of clinically occult high-risk oral premalignant disease using a simple hand-held device," Head & Neck **29**(1), 71–76 (2007).
33. G. W. Falk, "Autofluorescence Endoscopy," Gastrointestinal Endoscopy Clinics of North America **19**(2), 209–220 (2009).
34. M. Zargi, I. Fajdiga, and L. Smid, "Autofluorescence imaging in the diagnosis of laryngeal cancer," Eur. Arch. Otorhinolaryngol **257**(1), 17–23 (2000).
35. D. H. Kim, S. W. Kim, and S. H. Hwang, "Autofluorescence imaging to identify oral malignant or premalignant lesions: Systematic review and meta-analysis," Head & Neck **42**(12), 3735–3743 (2020).
36. K. Beaudette, J. Li, J. Lamarre, *et al.*, "Double-Clad Fiber-Based Multifunctional Biosensors and Multimodal Bioimaging Systems: Technology and Applications," Biosensors **12**(2), 90 (2022).
37. L. Wang, H. Y. Choi, Y. Jung, *et al.*, "Optical probe based on double-clad optical fiber for fluorescence spectroscopy," Opt. Express **15**(26), 17681–17689 (2007).
38. D. C. Adams, Y. Wang, L. P. Hariri, *et al.*, "Advances in Endoscopic Optical Coherence Tomography Catheter Designs," IEEE J. Sel. Top. Quantum Electron. **22**(3), 210–221 (2016).
39. R. A. Leitgeb and B. Baumann, "Multimodal Optical Medical Imaging Concepts Based on Optical Coherence Tomography," Front. Phys. **6**, 00114 (2018).
40. W. Drexler, M. Liu, A. Kumar, *et al.*, "Optical coherence tomography today: speed, contrast, and multimodality," J. Biomed. Opt. **19**(7), 071412 (2014).
41. H. Pahlevaninezhad, A. M. D. Lee, T. Shaipanich, *et al.*, "A high-efficiency fiber-based imaging system for co-registered autofluorescence and optical coherence tomography," Biomed. Opt. Express **5**(9), 2978–2987 (2014).
42. H. Pahlevaninezhad, A. M. D. Lee, G. Hohert, *et al.*, "Endoscopic high-resolution autofluorescence imaging and OCT of pulmonary vascular networks," Opt. Lett. **41**(14), 3209–3212 (2016).
43. B. Saleh and M. Teich, *Fundamentals of Photonics*, 3rd Edition (2019).
44. H. M. Presby, "Ultraviolet-excited fluorescence in optical fibers and performs," Appl. Opt. **20**(4), 701 (1981).
45. J. A. Udovich, N. D. Kirkpatrick, A. Kano, *et al.*, "Spectral background and transmission characteristics of fiber optic imaging bundles," Appl. Opt. **47**(25), 4560 (2008).
46. H. M. Presby, "Fluorescence profiling of single-mode optical fiber preforms," Appl. Opt. **20**(3), 446–450 (1981).

Biomedical Optics EXPRESS

47. A. C. B. Greenwood, A. Verma, J. Russett, *et al.*, "Near-IR photoluminescence at the photon level in a silica fiber patch cable," Opt. Lett. **50**(7), 2421–2424 (2025).
48. Schott North America, Inc., "TIE-36 Fluorescence of optical glass," (2022).
49. W. Geffken, "The molar absorption of different ions in glasses," Glastechn. berichte. **35**, 27 (1962).
50. J. S. Stroud, "Optical Absorption and Color Caused by Selected Cations in High-Density, Lead Silicate Glass," J. Am. Ceram. Soc. **54**(8), 401–406 (1971).
51. D. Ehrt, P. Ebeling, U. Natura, *et al.*, "Redox equilibria and ultraviolet radiation induced defects in glasses," (n.d.).
52. A. Engel, R. Haspel, and V. Rupertus, "Fluorescence metrology used for analytics of high-quality optical materials," in *Optical Metrology in Production Engineering* (SPIE, 2004), Vol. 5457, pp. 65–73.
53. S. L. Logunov, "Application of UV laser induced Ge-oxygen defect fluorescence for fibre characterisation," Electron. Lett. **43**(25), 1416–1417 (2007).
54. . "Thorlabs · Double-Clad Fiber," https://www.thorlabs.com/double-clad-fiber?tabName=Specs.
55. L. Xiang, R. Chen, J. T. M. Tan, *et al.*, "Identification and removal of system-induced autofluorescence in miniaturized fiber-optic fluorescence endoscopes," PNAS Nexus **4**(8), pgaf226 (2025).
56. R. Chen, F. Rothermel, R. Fitridge, *et al.*, "Low background fluorescence 3D-printed micro-lens for imaging of vulnerable atherosclerotic plaques," APL Photonics **10**(4), 0247546 (2025).
57. S. Johansson, A. Bukschat, D. Lönard, *et al.*, "Characterization of Autofluorescence in Optical Fibers for NV-based Sensing Applications," (2026).
58. "FORJ: Miniature Fiber Rotary Joints (MicroJx Series)," https://princetel.com/forj/single-channel-miniature-fiber-rotary-joint-mjx-series/.
59. The MathWorks Inc., "MATLAB version: 24.2.0.2863752 (R2024b) Update 5," (2024).
60. A. Formozov, A. Dieter, J. Lamarre, *et al.*, "Fused-fiber-photometry based on a low-autofluorescence wideband multimode circulator," Opt. Express **32**(25), 44958–44969 (2024).
61. H. M. Pask, R. J. Carman, D. C. Hanna, *et al.*, "Ytterbium-doped silica fiber lasers: versatile sources for the 1-1.2 /spl mu/m region," IEEE J. Sel. Top. Quantum Electron. **1**(1), 2–13 (1995).
62. "Thorlabs · FN96A Guide to Connectorization and Polishing of Optical Fibers," https://www.thorlabs.com/item/FN96A.
63. S. Girardeau-Hubert, C. Deneuville, H. Pageon, *et al.*, "Reconstructed Skin Models Revealed Unexpected Differences in Epidermal African and Caucasian Skin," Sci. Rep. **9**(1), 7456 (2019).
64. "HQ485lp emission filter," https://www.chroma.com/products/parts/hq485lp.
65. "FF01-510/84-25," https://www.idex-hs.com/store/product-detail/ff01_510_84_25/fl-004380?cat_id=semrock_optical_filters&node=individual_optical_filters.
66. B. Zhu, J. C. Rasmussen, Y. Lu, *et al.*, "Reduction of excitation light leakage to improve near-infrared fluorescence imaging for tissue surface and deep tissue imaging," Med. Phys. **37**(11), 5961–5970 (2010).
67. E. S. Pearson, ""Student" as Statistician," Biometrika **30**, 210–250 (1939).
68. L. Vaccaro, M. Cannas, V. Radzig, *et al.*, "Luminescence of the surface nonbridging oxygen hole center in silica: Spectral and decay properties," Phys. Rev. B **78**(7), 075421 (2008).
69. G. H. Sigel and M. J. Marrone, "Photoluminescence in as-drawn and irradiated silica optical fibers: an assessment of the role of non-bridging oxygen defect centers," J. Non-Cryst. Solids **45**(2), 235–247 (1981).
70. B. Li, J. Zhou, Y. Han, *et al.*, "Impact of heat treatment on NBOHC luminescence of OH-containing and H2-impregnated fused silica for deep-ultraviolet applications," J. Lumin. **209**, 31–38 (2019).
71. N. Uesugi, K. Noguchi, N. Hata, *et al.*, "Visible fluorescence from heat-treated GeO2-doped silica optical fibre in hydrogen atmosphere," Electron. Lett. **20**(25-26), 1068–1069 (1984).
72. R. Janani, D. Majumder, A. Scrimshire, *et al.*, "From acrylates to silicones: A review of common optical fibre coatings used for normal to harsh environments," Progress in Organic Coatings **180**, 107557 (2023).
73. P. R. Herz, Y. Chen, A. D. Aguirre, *et al.*, "Micromotor endoscope catheter for in vivo, ultrahigh-resolution optical coherence tomography," Opt. Lett. **29**(19), 2261–2263 (2004).
74. P. H. Tran, D. S. Mukai, M. Brenner, *et al.*, "In vivo endoscopic optical coherence tomography by use of a rotational microelectromechanical system probe," Opt. Lett. **29**(11), 1236–1238 (2004).
75. X. Attendu, P. R. Bloemen, N. H. Kind, *et al.*, "All-reflective tethered capsule endoscope for multimodal optical coherence tomography in the esophagus," J. Biomed. Opt. **29**(09), 096003 (2024).